



Modeling of helium bubble nucleation and growth in neutron irradiated boron doped RAFM steels

Christian Dethloff^{a,*}, Ermile Gaganidze^a, Vyacheslav V. Svetukhin^b, Jarir Aktaa^a

^a Karlsruhe Institute of Technology (KIT), Institute for Applied Materials, Hermann-von-Helmholtz-Platz 1, 76344 Eggenstein-Leopoldshafen, Germany

^b Ulyanovsk State University, Leo Tolstoy Str. 42, 432970 Ulyanovsk, Russian Federation

ARTICLE INFO

Article history:

Received 1 December 2010

Accepted 22 December 2011

Available online 29 December 2011

ABSTRACT

Reduced activation ferritic/martensitic (RAFM) steels are promising candidates for structural materials in future fusion technology. In addition to other irradiation defects, the transmuted helium is believed to strongly influence material hardening and embrittlement behavior. A phenomenological model based on kinetic rate equations is developed to describe homogeneous nucleation and growth of helium bubbles in neutron irradiated RAFM steels. The model is adapted to different ¹⁰B doped EUROFER97 based heats, which already had been studied in past irradiation experiments. Simulations yield bubble size distributions, whereby effects of helium generation rate, surface energy, helium sinks and helium density are investigated. Peak bubble diameters under different conditions are compared to preliminary microstructural results on irradiated specimens. Helium induced hardening was calculated by applying the Dispersed Barrier Hardening model to simulated cluster size distributions. Quantitative microstructural investigations of unirradiated and irradiated specimens will be used to support and verify the model.

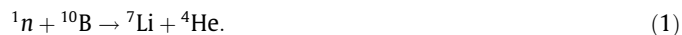
© 2012 Karlsruhe Institute of Technology. Published by Elsevier B.V. All rights reserved.

1. Introduction

Fusion technology was subject of many scientific studies during the last decades. In spite of large progress achieved in the development of fusion technology there are still many technological problems to be solved. Within these efforts materials research is a crucial task. Not only is it important to develop new structural materials that are capable to withstand the high neutron irradiation dose and heat flux in the fusion environment, but also high activation should be prevented.

Reduced activation ferritic/martensitic (RAFM) body-centered cubic (bcc) steels like the European EUROFER97 [1] are candidate structural materials for the First Wall and Breeding Blanket components of a future fusion reactor. The main alloying elements of EUROFER97 are shown in Table 1 [2]. Although ferritic/martensitic steels show less swelling than conventional austenitic stainless steels under neutron irradiation, the introduced microstructural damage will be severe taking into account the long lifetime of a fusion reactor. Frenkel pairs created by displacement cascades agglomerate to larger self-interstitial atom (SIA) clusters, voids (vacancy clusters) and dislocation loops. The production of helium by transmutation of iron or alloyed elements enhances the defect production by nucleation and growth of helium–vacancy clusters, leading to further degradation of the mechanical properties of the steel.

Generation of helium by transmutation depends strongly on the applied neutron energy spectrum during irradiation. Spallation neutron sources [3], e.g. produce much higher He-to-dpa ratios than expected under fusion conditions, along with high concentrations of hydrogen. In experimental fission reactors, damage rates comparable to fusion can be achieved, but helium generation is too low. Therefore, helium is often artificially introduced into the matrix. Besides helium ion implantation irradiation-induced transmutation of additional alloying elements [4] can be used for helium generation. In the latter case a homogeneous distribution of helium inside the matrix can be achieved, similar to the conditions expected in a fusion environment. Although the generation rates of helium may differ from expected ones, this method gives the possibility to simulate different helium production rates and contents. Boron is a potential element for this technique, because its isotope ¹⁰B, which is enclosed within natural boron at a fraction of 20 atomic percent, transmutes by a (n,α)-reaction into helium and lithium:



A drawback of the boron doping method is the difficulty of controlling the distribution of boron in the matrix, as it tends to precipitate or segregate at grain boundaries. Another drawback of this technique is a not yet identified role of the reaction product lithium. Lithium effects were shown to be minor by comparing the DBTT shifts in neutron irradiated boron doped and helium implanted F82H steel specimens in [5].

* Corresponding author.

E-mail address: christian.dethloff@kit.edu (C. Dethloff).

Table 1

Composition of EUROFER97 and boron doped steels ADS2 and ADS3 in weight percent (wt.%) (Fe balance) [2].

	Cr	W	Mn	V	Ta	C	B
EUROFER97	8.91	1.08	0.48	0.2	0.14	0.12	0.001
ADS2	9.31	1.27	0.602	0.19	0.055	0.109	0.0082 (nat. B)
ADS3	8.80	1.125	0.395	0.193	0.088	0.095	0.0083 (¹⁰ B)

Lacking an appropriate irradiation facility that is capable of providing a neutron energy spectrum comparable to fusion conditions (like the upcoming International Fusion Materials Irradiation Facility – IFMIF [6]) conventional experimental fission reactors are used. Irradiation facilities like the High Flux Reactor (HFR) in Petten used in the SPICE irradiation program [7,8] and BOR-60 at the Joint Stock Company “State Scientific Centre – Research Institute of Atomic Reactors” (JSC “SSC RIAR”) in Dimitrovgrad used for the ARBOR1 irradiation program [9] have different neutron spectra and hence different transmutation cross sections for boron. Therefore it is possible that steels with the same chemical composition create different amounts of helium only because of different ratios of stable boron isotopes ¹⁰B and ¹¹B and different irradiation conditions. In the irradiation programs SPICE and ARBOR1 helium effects were studied on different EUROFER97 based boron doped steels, which were produced by the materials development group at KIT [2]. The compositions of alloys ADS2 and ADS3 (given in weight per cent) are shown in Table 1. Boron doped as well as reference EUROFER97 steels got similar heat treatments of 1040 °C for 0.5 h + 760 °C for 1.5 h. Helium contents due to boron transmutation at the end of irradiation in the different irradiation programs are shown in Table 2. In the SPICE program all boron is burnt up during the irradiation process, whereas in ARBOR1 a high fraction of boron still remains in the matrix, although the material suffered nominally higher damage.

To check the distribution of boron in the model alloy microstructural investigations were performed by Auger electron spectroscopy (AES) and transmission electron microscopy (TEM) by applying Energy Filtered Transmission Electron Microscopy (EFTEM) technique [11] on unirradiated ADS3 specimens. Only a few isolated boron-nitride precipitates were found in the matrix of the model alloy with 83 wppm ¹⁰B. Boron segregation at grain boundaries or other defects was not observed, and most of the boron was estimated to be uniformly distributed in the steel matrix below the EFTEM detectable limit. Thus preferential helium transmutation at microstructural defects seems to have only minor influence on bubble nucleation for the considered alloys, a finding that is also supported by TEM investigations on irradiated samples. Specimens of ADS3 were studied after low temperature irradiation at 250 °C in SPICE (13.6 dpa) [12,13] and at 335 °C in ARBOR1 (22.4 dpa) [14]. Evaluation of the micrographs showed homogeneously distributed helium bubbles throughout the matrix, mostly with sizes of less than 5 nm for both experiments. By contrast, after irradiation at higher temperatures of 450 °C to 18.1 dpa in SPICE

[12, Fig.7], most bubbles are located at lattice defects like line dislocations and grain boundaries, but this effect might be attributed to a higher helium diffusivity increasing the diffusion current to sinks. Further quantitative TEM investigations on irradiated SPICE and ARBOR1 specimens are scheduled and will provide helium bubble size distributions after different irradiation conditions.

Many experimental studies were dedicated to hardening and embrittlement of RAFM steels under irradiation from different particle sources [3,15,16]. Through boron doping with varying isotope ratios the effects of different helium concentrations on hardening and embrittlement could be easily observed due to a separation from other microstructural influences in [10], where instrumented impact tests were performed on EUROFER97 and boron doped steels. In comparison with EUROFER97, ADS2 and ADS3 show only a small increase in the Ductile-to-Brittle Transition Temperature (DBTT) and a slightly lower Upper Shelf Energy (USE) in the unirradiated condition. Therefore, the alloying effect of boron on the mechanical properties in the applied doping range was considered insignificant. It has to be mentioned that a specially prepared cast (ADS4) with 0.112 wt.% ¹⁰B yielding 5580 appm helium showed degraded impact properties even in the unirradiated condition and was not taken into account.

After irradiation in SPICE experiment the boron doped steels show severe embrittlement and hardening at low irradiation temperatures ($T_{irr} \leq 350$ °C). At $T_{irr} = 250$ °C and a dose of 13.6 dpa the hardening and embrittlement is compared to the basic EUROFER97 yielding an extra embrittlement ($\Delta DBTT_{He}$) and hardening ($\Delta \sigma_{He}$) due to boron-helium transmutation. While EUROFER97 suffered a hardening of 405 MPa and a DBTT shift of 150 °C, additionally produced 84 appm helium in ADS2 yields $\Delta \sigma_{He}$ of 40 MPa and $\Delta DBTT_{He}$ of 120 °C. ADS3 with 432 appm helium showed an extra hardening of 92 MPa and extra embrittlement of 220 °C compared to irradiated EUROFER97. The role of the simultaneously generated lithium is not exactly known, but the influence is supposed to be small. It was found that at higher temperatures ($T_{irr} = 450$ °C) $\Delta DBTT$ decreases again, for ADS2 it even vanishes.

Due to the close correlation between helium generation, microstructural changes and mechanical properties it is important to understand and describe the influence of helium. Despite extensive modeling efforts in the field of radiation effects in fusion reactor materials [17], until now helium behavior has mainly been described on small time and length scales, e.g. by *ab initio* calculations [18], by Kinetic Monte-Carlo simulations [19] and by Molecular Dynamics (MD) simulations, considering helium-defect interactions, e.g. mutual reactions of helium with dislocations and grain boundaries [20]. Results obtained in this way serve as input parameters for simulation methods on larger time and length scales within a multiscale modeling approach [21]. Among other multiscale simulation methods, kinetic rate theory allows the description of helium bubble nucleation in the range of seconds as well as bubble growth up to time scales of years.

Describing clustering by mutual reaction equations is well known in literature, especially for void growth [22], and also underlying helium effects on void growth and helium clustering were studied [23,24]. Bubble to void transformation was predicted in [22] when the number of helium atoms in a bubble exceeds a critical number for given irradiation conditions. Bimodal size distribution of helium bubbles often observed in neutron irradiation and helium implantation experiments is a clear manifestation of bubble to void transformation. Taking into account the accumulated knowledge we developed a rate theory model suited for the description of bubble nucleation and growth phase, and tailored it to irradiation experiments on boron doped steels.

This publication is structured as follows: in Section 2 the model is derived and explained. While Section 3 presents simulation conditions and results, Section 4 shows the assessment of the helium

Table 2

Boron content of EUROFER97 and boron doped steels ADS2 and ADS3 and associated cumulative helium content due to boron transmutation in SPICE and ARBOR1 irradiation programs [10].

	Boron (wt.%)	Helium (appm)	
		SPICE	ARBOR1
EUROFER97	0.001	10.2	–
ADS2 (nat. B)	0.0082	83.6	6.2
ADS3 (¹⁰ B)	0.0083	432.0	43.3

induced hardening. Results are discussed in Section 5, and Section 6 concludes and gives an outlook.

2. Model description

2.1. Basic equations

The developed model is based on the theory of homogeneous nucleation [25] as a result of the decay of a supersaturated solid solution. Generally, a monomer M is captured or emitted by a cluster M_i , which contains i particles. This process takes place with a certain probability expressed by kinetic rate coefficients k_i for capturing and g_{i+1} for emitting a monomer:



Clustering of helium atoms in solids cannot be easily described due to the strong binding of helium to several microstructural defects, e.g. vacancies or voids, grain boundaries, etc. From energetical considerations helium prefers to occupy a substitutional lattice site and thus forms helium–vacancy clusters. Therefore the role of vacancies and the diffusion of different helium–vacancy clusters also has to be considered when describing nucleation and growth of helium bubbles. In spite of extensive theoretical and experimental investigations (see Paragraph Section 2.3), there still exists no consensus on the dominant helium diffusion mechanism, which is expected to show a strong temperature dependence. Moreover, there exists only rare and partly inconsistent information about the helium density (helium-to-vacancy ratio) in a bubble [26,27]. In this work calculations are performed for a helium-to-vacancy ratio x_{He} of 1 and 0.5, being constant for all bubble sizes within one simulation. Assumption of a constant x_{He} is still a reasonable approximation for the description of the bubble growth at an early stage, i.e. prior to bubble to void transformation. The values of x_{He} are furthermore justified by two considerations:

1. Molecular dynamic and static calculations in [28] yield the lowest energy configuration (formation energies) of helium bubbles for the helium-to-vacancy ratio of approximately unity.
2. Electron Energy Loss Spectroscopy (EELS) in the TEM has been used for the study of helium state in helium bubbles in irradiated ADS3 [14]. Results showed that the helium density inside of one of the largest bubble found (4 nm) corresponds to a helium-to-vacancy ratio of ~ 0.3 . The TEM investigation, furthermore yielded unimodal bubble size distribution with no sign for transformation from bubble to unstable void growth regime.

Considering only single mobile defects in the matrix, the change in cluster concentrations $C_i(t)$ of different sizes i with time t can be expressed by the following set of differential equations:

$$\frac{\partial C_1(t)}{\partial t} = G_{\text{He}}(t) - L_{\text{sinks}}(t) - \sum_i k_i C_1(t) C_i(t) + \sum_i g_i C_i(t) \quad (3)$$

and

$$\frac{\partial C_i(t)}{\partial t} = -[k_i C_1(t) + g_i] C_i(t) + g_{i+1} C_{i+1}(t) + k_{i-1} C_1(t) C_{i-1}(t), \quad (4)$$

both valid for $i \geq 2$. Eq. (3) describes the time evolution of the monomer concentration $C_1(t)$ by considering the helium generation rate $G_{\text{He}}(t)$, the loss rate to sinks $L_{\text{sinks}}(t)$ and catching and emitting of a monomer by existing clusters. G_{He} and L_{sinks} will be defined later. While Eq. (3) provides the left boundary condition for the numerical calculation carried out by a Fortran code, the first term of the Master Eq. (4) describes the decrease of the concentration

of clusters with size i due to growing and shrinking, while the second and third term lead to an increase in cluster quantity by providing shrinking of larger and growth of smaller clusters, respectively.

2.2. Cluster radius

The considered iron lattice features a bcc structure, therefore an elementary cell with lattice constant a_{Fe} owns two atoms on a regular lattice site. The atomic volume Ω can be expressed by $\Omega = 0.5a_{\text{Fe}}^3$. A volume occupied by one helium atom in a cluster, V_1 depends on the helium-to-vacancy ratio x_{He} , and can be given by $V_1 = \Omega/x_{\text{He}}$. Helium clusters are assumed to be spherical. Their volume, V_i containing i monomers is defined by $V_i = \frac{4}{3}\pi R_i^3 = iV_1$. By this means, the cluster radius R_i is given by

$$R_i = \sqrt[3]{\frac{3\Omega i}{4\pi x_{\text{He}}}} = b\sqrt[3]{i}, \quad (5)$$

with a parameter b defined as an equivalent monomer radius. In [29] temperature dependent lattice constants are calculated for 10% chromium alloyed iron, which will be used for simulations in this work.

2.3. Effective helium diffusivity

For determining the effective helium diffusivity one has to consider which helium diffusion mechanism takes place under irradiation. Calculations of helium energetics are used to get an idea of the most likely diffusion mechanism. The migration energy of interstitial helium He_i is quite low (0.06 eV) [30]. Nevertheless, helium has a high tendency to be trapped by vacancies (V), which leads to substitutional helium (He_iV_1) with a high binding energy of substitutional helium to vacancy of 2.3 eV. Possible diffusion paths are then given by a dissociation mechanism, i.e. jumping to an interstitial position and further interstitial migration, or by migration via vacancies. Migration energies thereby depend strongly on the vacancy concentration. For a high vacancy supersaturation, which in our case is expected due to high point defect generation at low temperature irradiation conditions, migration through a helium–divacancy mechanism was shown to own the lowest effective migration energy of 0.3 eV [18], which is therefore assumed to be the dominant diffusion mechanism taking place. We are aware that other vacancy mediated mechanisms will also contribute in the evolution of microstructure, however, corresponding diffusivities will be at most comparable to that of the helium divacancy mechanism [19].

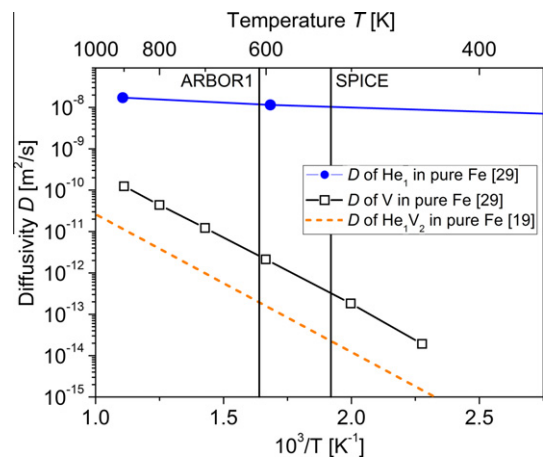


Fig. 1. Temperature dependent diffusivities of interstitial helium He_i , vacancies V and helium–divacancies He_iV_2 calculated by [19,29]. Vertical lines show relevant temperatures of SPICE and ARBOR1 irradiation experiments.

Fig. 1 shows temperature dependent diffusion coefficients of interstitial helium, vacancies and helium–divacancy clusters, calculated by atomistic molecular dynamics simulations [29] and kinetic Monte-Carlo simulations using *ab initio* input data [19]. While interstitial helium diffusion is quite fast, trapping of helium by vacancies under irradiation conditions lowers its diffusivity below the diffusion coefficient for single vacancies for a helium–divacancy mechanism. The effective helium diffusivity $D_{\text{He}}^{\text{eff}}$ used in this model is taken as a fitting parameter close to values of the helium–divacancy diffusion coefficient shown in Fig. 1.

2.4. Kinetic rate coefficients

2.4.1. Capture rate coefficient k_i

To solve the Master Eq. (4) the kinetic rate coefficients have to be defined. Basically, monomer capturing by a cluster involves diffusion of monomers to clusters and an attaching reaction [31]. Since an attachment barrier is believed to have only minor influence on clustering of helium atoms, the capture rate in this model uses diffusion as the governing process for cluster growth. The capture rate k_i is described by the effective diffusion coefficient and by geometrical parameters A_i for active surface and by effective radius R_{eff} . In the region within this radius the cluster is capable of capturing a monomer.

$$k_i = \frac{A_i}{R_{\text{eff}}} D_{\text{He}}^{\text{eff}}. \quad (6)$$

In this model helium clusters are assumed to be spherical. Therefore the geometrical parameters are adapted.

$$A_i = 4\pi R_i^2, \quad (7)$$

$$R_{\text{eff}} = R_i. \quad (8)$$

Inserting Eqs. (7) and (8) in (6) yields the diffusion governed capture rate:

$$k_i = 4\pi R_i D_{\text{He}}^{\text{eff}}. \quad (9)$$

2.4.2. Emission rate coefficient g_{i+1}

The emission rate g_{i+1} of monomers from clusters is described under the assumption of steady state condition, which implies equality of monomer capturing and emitting probabilities:

$$g_{i+1} C_{i+1}^{\text{eq}} = k_i C_1^{\text{eq}} C_i^{\text{eq}}. \quad (10)$$

The concentrations in Eq. (10) can be replaced by the atomic density of the iron lattice (expressed by the reciprocal of the atomic volume Ω) and atomic fractions x_j of the different defects j , i.e.

$$g_{i+1} = k_i \left[C_1 \frac{C_i}{C_{i+1}} \right]_{\text{eq}} = k_i \Omega^{-1} \left[x_1 \frac{x_i}{x_{i+1}} \right]_{\text{eq}}. \quad (11)$$

The relation of the fractions x_j can be expressed by the following equation analog to [32]:

$$\left[\frac{x_1 x_i}{x_{i+1}} \right]_{\text{eq}} = \left[\frac{\theta_1 \theta_i}{\theta_{i+1}} \right]_{\text{eq}} \exp \left[-\frac{G_1^f + G_i^f - G_{i+1}^f}{k_B T} \right]. \quad (12)$$

Therein, θ_j are the internal degrees of freedom for defects j , G_j^f the Gibbs free energies of formation of a defect cluster containing j monomers, herein after referred to as formation energies. The relation of the internal degrees of freedom are assumed as 1 [33]. The equilibrium concentration of monomers is obtained by statistical thermodynamics [34]:

$$C_1^{\text{eq}} = \Omega^{-1} \exp \left[-\frac{G_1^f}{k_B T} \right]. \quad (13)$$

Combination of Eqs. (10)–(13) yields the equation for the emission rate g_{i+1} as a function of the formation energy difference of size adjacent clusters:

$$g_{i+1} = k_i C_1^{\text{eq}} \exp \left[\frac{G_{i+1}^f - G_i^f}{k_B T} \right]. \quad (14)$$

As mentioned previously, formation energies can be obtained for different cluster sizes, e.g. by molecular dynamics calculations [28]. Nevertheless, the effort of calculation is quite high, that is why only formation energies for small clusters (less than 100 helium atoms) are available in the literature. In the following paragraph a macroscopic material constant, the surface energy γ_{SF} (of iron) [35–38], is introduced, which is assumed to be independent of the cluster size i and which replaces the formation energies in the emission rate coefficient.

Cluster formation energy G_i^f and nucleation energy G_i^n are connected to each other as shown next:

$$G_i^n = G_i^f - i G_1^f. \quad (15)$$

Following classical nucleation theory [39], the nucleation of a new phase affects the Gibbs free energy of the system in two opposing ways: the energy is lowered because of the nucleation of a new homogeneous volume while the creation of an interface between the two phases increases the Gibbs free energy

$$G_i^n = -G_1^f i + \gamma_i i^{\frac{2}{3}}. \quad (16)$$

The first term on the right-hand side of Eq. (16) shows the contribution of the volume, the second one gives the surface term depending on the surface energy per cluster atom γ_i . The differences of the nucleation energies of clusters with size i and $i+1$ can be expressed by the derivative of Eq. (16) with respect to i :

$$G_{i+1}^n - G_i^n \approx \frac{dG_i^n}{di} \Delta i = -G_1^f + \frac{2}{3} \gamma_i i^{-\frac{1}{3}}. \quad (17)$$

Including Eqs. (13), (15), (17) into (14) yields the emission rate coefficient depending on the surface energy per cluster atom γ_i :

$$g_{i+1} = k_i C_1^{\text{eq}} \exp \left[\frac{\frac{2}{3} \gamma_i i^{-\frac{1}{3}}}{k_B T} \right]. \quad (18)$$

The surface term of Eq. (16) can be related to the surface energy γ_{SF} :

$$\begin{aligned} \gamma_i i^{\frac{2}{3}} &= \gamma_{\text{SF}} \cdot 4\pi R_i^2 \\ \gamma_i &= 4\pi R_i^2 i^{-\frac{2}{3}} \gamma_{\text{SF}}. \end{aligned} \quad (19)$$

Inserting Eq. (19) into (18), the emission rate coefficient can be expressed with the macroscopic material parameter γ_{SF} by the following equation:

$$g_{i+1} = k_i C_1^{\text{eq}} \exp \left[\frac{2\Omega \gamma_{\text{SF}}}{b^{\frac{2}{3}} i^{\frac{1}{3}} \cdot k_B T} \right]. \quad (20)$$

It has to be emphasized that Eq. (20) yields a size dependent emission rate coefficient where smaller clusters have a higher tendency to emit a monomer and therefore are more likely to shrink than larger clusters leading to a coarsening mechanism similarly described in [27].

2.5. Helium solubility

For the description of the kinetic coefficients the solubility (or equilibrium concentration) C_1^{eq} of helium in the iron matrix must be obtained. In principle, helium atoms in solution and in gas

phase have to be in equilibrium. By equalizing their chemical potentials as shown in [40], helium solubility can be calculated. Although the use of the chemical potential in the real gas phase would be a standard approach for solubility calculation, we have used an ideal gas approximation for estimation of solubility which was a starting point for a parametric study of its influence on the bubble evolution. An approximation for an ideal gas is described in [41] and can be expressed by

$$C_1^{eq} = X \frac{p_{He}}{p_0} \exp \left[\frac{S_F}{k_B} \right] \exp \left[-\frac{G_1^f}{k_B T} \right], \quad (21)$$

where X is the number of possible positions of helium atoms per number of unit cell atoms of the iron lattice, p_{He} the helium bubble pressure and p_0 the standard pressure (in N/m²) as given by Eqs. (22) and (23), respectively, with helium mass m and Planck constant h .

$$p_{He} = \frac{2\gamma_{SF}}{R_i}, \quad (22)$$

$$p_0 = \frac{(k_B T)^{\frac{5}{2}} (2\pi m)^{\frac{3}{2}}}{4 \times 10^{-10} \cdot h^3}. \quad (23)$$

Eq. (21) is applicable to describe the equilibrium of free helium gas from bubbles with solvent helium in the solid at substitutional ($X = 1$) as well as interstitial position ($X = 6$), using the appropriate defect formation energies of $G_{1,sub}^f = 3.25$ eV and $G_{1,int}^f = 5.25$ eV [42], respectively. For the latter case, recent *ab initio* calculations of helium in bcc iron showed that the tetrahedral interstitial configuration is most stable [18]. The formation entropy S_F is calculated by the Sackur–Tetrode equation for ideal gases [43]:

$$S_F = k_B i \left[\frac{5}{2} + \ln \frac{(k_B T)^{\frac{5}{2}} (2\pi m)^{\frac{3}{2}}}{4 \cdot 10^{-10} \cdot p_{He} h^3} \right]. \quad (24)$$

Since solubility to interstitial positions is much lower, substitutional solubility C_1^{eq} was calculated for the irradiation experiments' relevant temperatures, as shown in Table 5, and is used for simulations.

2.6. Loss rate at sinks

Single helium atoms may be caught by sinks and will not take part in further clustering in the matrix. Lattice defects like dislocations, interstitial loops and vacancy clusters, but also precipitates and grain boundaries, can act as sinks for helium atoms. In this paragraph a general expression is presented describing the loss rate L_{sinks} of monomers at sinks [44]:

$$L_{sinks} = D_{He}^{eff} C_1(t) k_{sinks}^2. \quad (25)$$

The loss rate is proportional to the diffusivity of the monomer and its concentration. The sink strength k_{sinks}^2 sums up all sink strengths of existing defects j in the matrix and can be expressed by

$$k_{sinks}^2 = \sum_j k_j^2. \quad (26)$$

Table 3

Sink strengths of different defects. Z_{He} is the bias factor, ρ_{disl} the dislocation density, R_{loop} the interstitial loop radius, C_{loop} the interstitial loop concentration, and R_{grain} is the grain radius.

Sink j	Sink strength k_j^2	
Line dislocation	$Z_{He} \rho_{disl}$	[45]
Interstitial loop	$4\pi R_{loop} C_{loop}$	[46]
Spherical grain boundary	$15/R_{grain}^2$	[47]

Sink strengths for various defects can be derived from [45–47] and are shown in Table 3.

3. Simulations

3.1. Helium generation rates

Simulations are adapted to boron doped alloys ADS2 and ADS3 irradiated in SPICE and ARBOR1 experiments. As shown earlier the left boundary condition has to be specified by the helium generation rate characteristic for the different irradiation conditions.

The concentration of generated helium in the steel matrix is calculated by the equation

$$C_1^{He}(t) = C_{10B}^{max} \left(1 - \exp \left[-\frac{G_{dpa} \cdot t}{G_{dpa}^0} \right] \right) + G_{matrix} G_{dpa} \cdot t. \quad (27)$$

Therein, C_{10B}^{max} is the ¹⁰B content, G_{dpa} is the damage rate, G_{dpa}^0 is the neutron spectrum characteristic damage constant for ¹⁰B transmutation, and G_{matrix} is the transmutation rate of other helium producing isotopes in the steels and t the irradiation time. The values for the different irradiation parameters are shown in Table 4. Fig. 2 shows the cumulative helium concentration calculated by Eq. (27) for both boron doped alloys irradiated in SPICE and ARBOR1. The boron transmutation in the SPICE experiment already ceases after 10^7 s. Additional helium is only generated by transmutation of other elements in the steel matrix. The final helium content after 6.67×10^7 s of irradiation in SPICE is about 439 and 91 appm for ADS3 and ADS2, respectively. The situation differs for the boron transmutation in the ARBOR1 experiment: due to the low transmutation cross section of ¹⁰B for fast neutrons the generated helium concentration is quite low in comparison to SPICE. Thus the transmutation of steel matrix elements has a higher influence on the cumulative helium content, leading to 50 and 13 appm for ADS3 and ADS2 at the end of irradiation after 3.98×10^7 s, respectively. In the case of ADS2 in ARBOR1 almost the same amounts of helium are produced by ¹⁰B and steel matrix elements.

3.2. Nucleation of helium clusters

A matter of particular interest is the nucleation process of helium clusters, i.e. how nucleation and further growth of clusters go hand in hand. Fig. 3 shows the cumulative generated helium, the helium monomer concentration, cluster content and cluster density for short irradiation times. Calculations are performed for ADS3 in SPICE experiment with standard parameters listed in Table 5 and helium-to-vacancy ratio x_{He} of 1. The maximum helium concentration is limited by the cumulative generated helium (curve 1), and partitioned into monomer and cluster content. The helium monomer concentration (curve 2) is peaked at 73 s. For times smaller than 10 s, all generated helium exists as single helium atoms and contributes to the nucleation phase. At the maximum of the monomer concentration the same amount of helium is already bound to clusters (curve 3) indicating a di-atomic nucleation mechanism of helium bubbles in accordance with [27]. After this time the helium monomer concentration in the matrix decreases, i.e. it is more and more likely that a newly generated helium atom is added to an existing cluster than to find another monomer for di-atomic nucleation. Therefore, the cluster density (curve 4) shifts away from the total helium concentration and starts to saturate.

The development of the mean cluster size (dashed curve) confirms this statement. The mean number of helium atoms in the clusters already increases from 1 at 10 s to about 1.4 at 73 s, when the monomer concentration peaks, and reaches 2 after 138 s of irradiation.

Table 4

Parameters of helium generation and irradiation programs. Parameters for the irradiation experiment SPICE are taken from [48,49], ARBOR1 parameters from [50].

Parameter	Unit	SPICE		ARBOR1	
		ADS2	ADS3	ADS2	ADS3
C_{10B}^{max}	appm	84	432	84	432
G_{dpa}	dpa/s	2.045×10^{-7}		5.620×10^{-7}	
G_{dpa}^0	dpa	0.34		212.30	
G_{matrix}	appm/dpa	0.54		0.29	
Irradiation time	s	6.67×10^7		3.98×10^7	
Cumulative damage	dpa	13.6		22.4	
Irradiation temperature T	K	523.15		611.15	

3.3. Time dependence of cluster size distribution

The time dependent evolution of the cluster size distribution is examined. Cluster densities of different cluster sizes derived for characteristic irradiation times of ADS3 in SPICE are compared in Fig. 4. At short irradiation times of 10^4 s one nanometer sized bubbles with a density of 10^{20} m^{-3} exist. With further irradiation the bubble distribution peak shifts to larger sizes and the cluster densities decrease. At the end of irradiation after 6.67×10^7 s, the calculated bubble size distribution is peaked at a diameter of 4.6 nm with a cluster density of $1.4 \times 10^{19} \text{ m}^{-3}$. At 10^6 s, the ^{10}B transmutation is still in progress, therefore new helium is added

to the matrix leading to an increase of small cluster sizes as it is shown in the diagram. At the end of irradiation densities of small clusters strongly decrease because helium bubbles tend to coarsen due to the size dependent helium resolution mentioned in Section 2.4.2. With good agreement, the calculated bubble peak diameters are comparable to preliminary results of microstructural TEM investigations of ADS3 after SPICE irradiation [12,13], while quantitative measurements are currently in progress.

3.4. Influence of surface energy

It was shown in Section 2.4.2, that the size dependent emission rate constant yields a coarsening mechanism, where smaller clusters tend to shrink for the benefit of larger ones. The question arises, how the surface energy and hence the emission rate constant directly influence the final cluster size distribution. Fig. 5 shows the calculated cluster densities in ADS3 at the end of the ARBOR1 irradiation experiment with simulation parameters given in Table 5 ($x_{\text{He}} = 1$) and with surface energies of 1 and 2.318 J/m². As expected, a higher surface energy γ_{SF} of 2.318 J/m² derived from [38] for a ARBOR1 irradiation temperature of 611 K shifts the cluster size distribution to larger clusters, while the densities of smaller clusters decrease (illustrated by arrows).

3.5. Helium bubble evolution in SPICE and ARBOR1

Final cluster size distributions at the end of irradiation of ADS2 and ADS3 for SPICE and ARBOR1 experiments are calculated with characteristic helium generation rates and irradiation parameters for $x_{\text{He}} = 1$. The corresponding simulation results are shown in Fig. 6 (continuous lines). In the case of SPICE irradiation the final bubble size distributions peak after 6.67×10^7 s at bubble diameters of 3.7 and 4.6 nm for ADS2 and ADS3, respectively. The peak concentrations are two orders of magnitude higher than those for the ARBOR1 specimens due to the different helium generation rates and helium contents. The final peak bubble diameters for

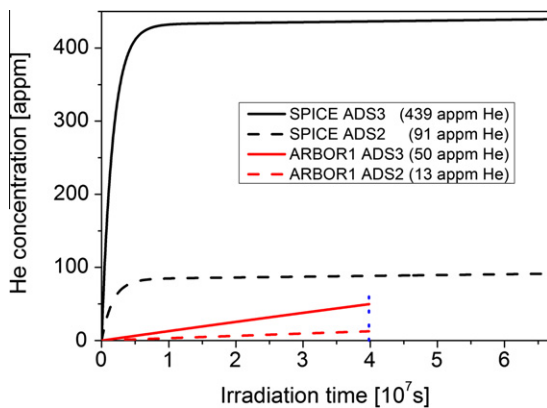


Fig. 2. Generated helium in boron doped alloys ADS2 and ADS3 during irradiation in SPICE and ARBOR1 programs calculated by Eq. (27). Given values show final helium concentration at the end of irradiation.

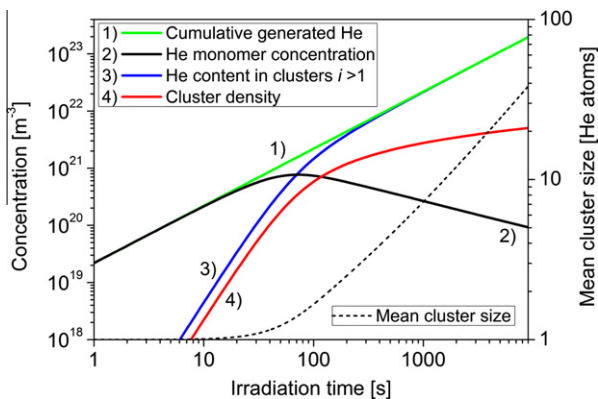


Fig. 3. Nucleation phase and further growth of helium clusters in ADS3 at short irradiation times in SPICE experiment. The evolution of generated helium, helium monomer concentration, cluster content and cluster density are shown for $x_{\text{He}} = 1$. The mean cluster size is calculated and given by the dashed line.

Table 5

Standard simulation parameters for SPICE and ARBOR1 relevant temperatures.

Parameter	Unit	SPICE	ARBOR1	Ref.
T	K	523.15	611.15	–
γ_{SF}	J/m ²	2.332	2.318	[38]
a_{Fe}	nm	0.2875	0.2879	[29]
$C_{\text{Fe}}^{\text{eq}}$	m ⁻³	5.01×10^{-2}	1.61×10^3	Eq. (21)
$D_{\text{He}}^{\text{eff}}$	m ² /s	8.0×10^{-15}	2.4×10^{-14}	Fit [19]
μ	GPa	77.2	73.2	[51]
b_{dist}	nm	0.2490	0.2493	–
G_{Fe}^{f}	eV	3.25		[42]
Z_{He}	–	~1		[44]
ρ_{dist}	m ⁻²	1.1×10^{14}		[11]
R_{grain}	μm	10		[52]
M_T	–	3.06		[53]

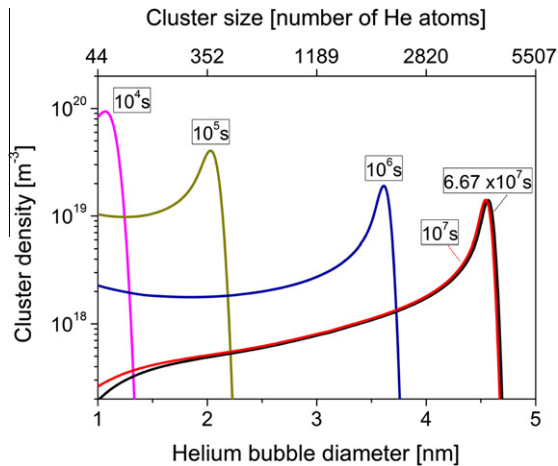


Fig. 4. Cluster size distributions for different irradiation times calculated for ADS3 in SPICE experiment ($x_{\text{He}} = 1$). The bubble diameter is given in nanometer, while the top scale shows corresponding cluster sizes in units of helium atoms.

the ARBOR1 calculations yield 6.9 and 7.9 nm for ADS2 and ADS3, respectively, after 3.98×10^7 s. In ARBOR1 irradiation the bubbles are larger than in SPICE, which can be attributed to a higher irradiation temperature influencing the material parameters. The temperature was taken into account by estimating the helium diffusivity to a higher value (see Table 5) based on Fig. 1. While the helium generation by boron transmutation already ceases after 10^7 s for the SPICE experiment, only about 7–10% of the boron in ARBOR1 specimens is burnt up at the end of irradiation, leading to almost constant transmutation rates during the whole ARBOR1 irradiation experiment of 3.98×10^7 s. This circumstance is also observable in Fig. 6: while for the SPICE specimens the concentrations drop at small bubble sizes, the ARBOR1 specimens show an increase in concentrations at small bubble sizes due to a continuous boron burn-up.

3.6. Influence of sinks

Grain boundaries (GBs) and line dislocations (LDs) are considered as sinks for helium, while for the latter case a bias factor Z_{He} of 1 is assumed [44]. With a grain size of $20 \mu\text{m}$ [52] and a dislocation density of $1.1 \times 10^{14} \text{ m}^{-2}$ measured by TEM [11] for unirradiated ADS3 the influences of sinks on helium bubble nucleation and final size distribution are determined.

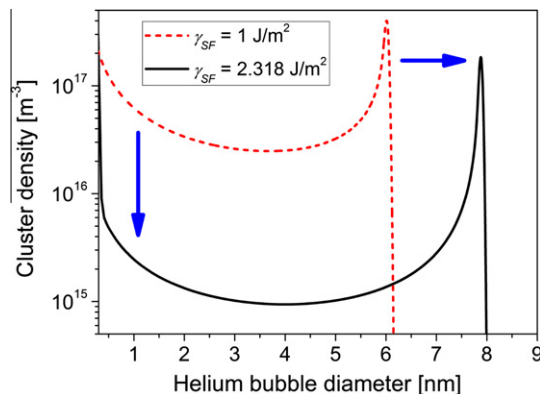


Fig. 5. Calculated final cluster size distributions ($x_{\text{He}} = 1$) in ADS3 after ARBOR1 irradiation, showing the effect of an increased surface energy γ_{SF} due to its influence on the emission rate constant and hence the size dependent helium cluster resolution (indicated by arrows).

Evolution of relevant concentrations are shown in Fig. 7 for ADS2 in SPICE (a, b) and ARBOR1 (c, d). While absolute concentrations are given in Fig. 7a and c, b and d show concentrations normalized to the helium concentration generated so far. When considering sinks for helium, the evolution of concentrations shows a different behavior than presented in Fig. 3. For the SPICE experiment, the development of monomers, cluster content and cluster density is only slightly influenced by the amount of helium captured at sinks (Fig. 7a), because only a small fraction of helium is trapped at both GB and LD sinks. The relative concentration of helium at sinks peaks after 372 s with a total fraction of 8%, and decreases down to 0.3% and an absolute amount of 0.3 appm at the end of irradiation. For ADS2 in ARBOR1, sinks have a great influence on the evolution of concentrations. After about 7500 s, 86% of the generated helium is captured by both sink types (Fig. 7d) leading to a decrease in cluster nucleation and bubble growth rates (Fig. 7c). When the helium monomer concentration in the matrix decreases again, the additional capture of helium by sinks starts to saturate due to the dependence of the sink loss rate on the monomer concentration in Eq. (25). Higher temperatures in ARBOR1 increase the fraction of helium at sinks due to the higher diffusivity, yielding a total helium fraction at sinks of 7.2% (equivalent to 1 appm) at the end of irradiation. For both irradiation experiments grain boundaries show a higher sink strength than line dislocations based on the used simulation parameters measured by mentioned TEM investigations on ADS3.

Fig. 6 compares the final bubble size distributions resulting from simulations with and without consideration of GB and LD sinks for a helium-to-vacancy ratio of 1. For the SPICE specimens sinks show no influence on size distributions, the calculations yield congruent results. For the ARBOR1 specimens, however, final bubble size distributions change (dashed lines). When taking into account sinks, size distributions are broadened and peaks are shifted towards larger bubble diameters with lower cluster densities. A larger peak shift is observed for ADS2, where the helium generation rate and helium content are lower. Final peak bubble diameters are 7.3 and 8.1 nm for ADS2 and ADS3, respectively.

This effect is attributed to the change in nucleation process, where the concentration of monomers is reduced by the amount of helium trapped at sinks. Therefore the number of nucleation centers decreases leading to lower cluster densities and larger diameters.

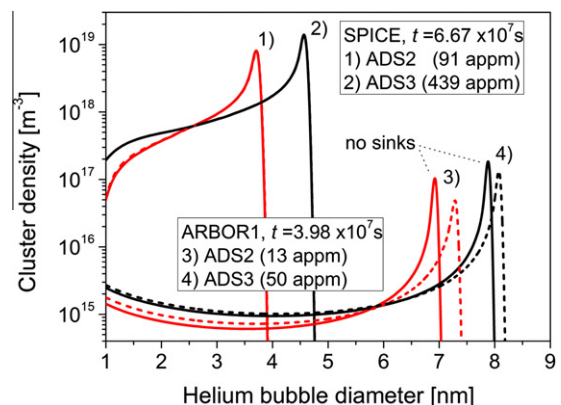


Fig. 6. Simulations of final cluster size distributions in SPICE and ARBOR1 irradiation experiments for the given irradiation times. Calculations are performed for boron doped steels ADS2 and ADS3 with characteristic helium generation rates and standard simulation parameters (Table 5, $x_{\text{He}} = 1$). Cumulative generated helium is given for each simulation analog to Fig. 2. While continuous lines show simulation results without taking into account sinks, dashed lines present simulations considering grain boundaries and line dislocations as sinks for helium. For the SPICE specimens sinks have no influence on the final bubble size distribution, hence the curves are congruent.

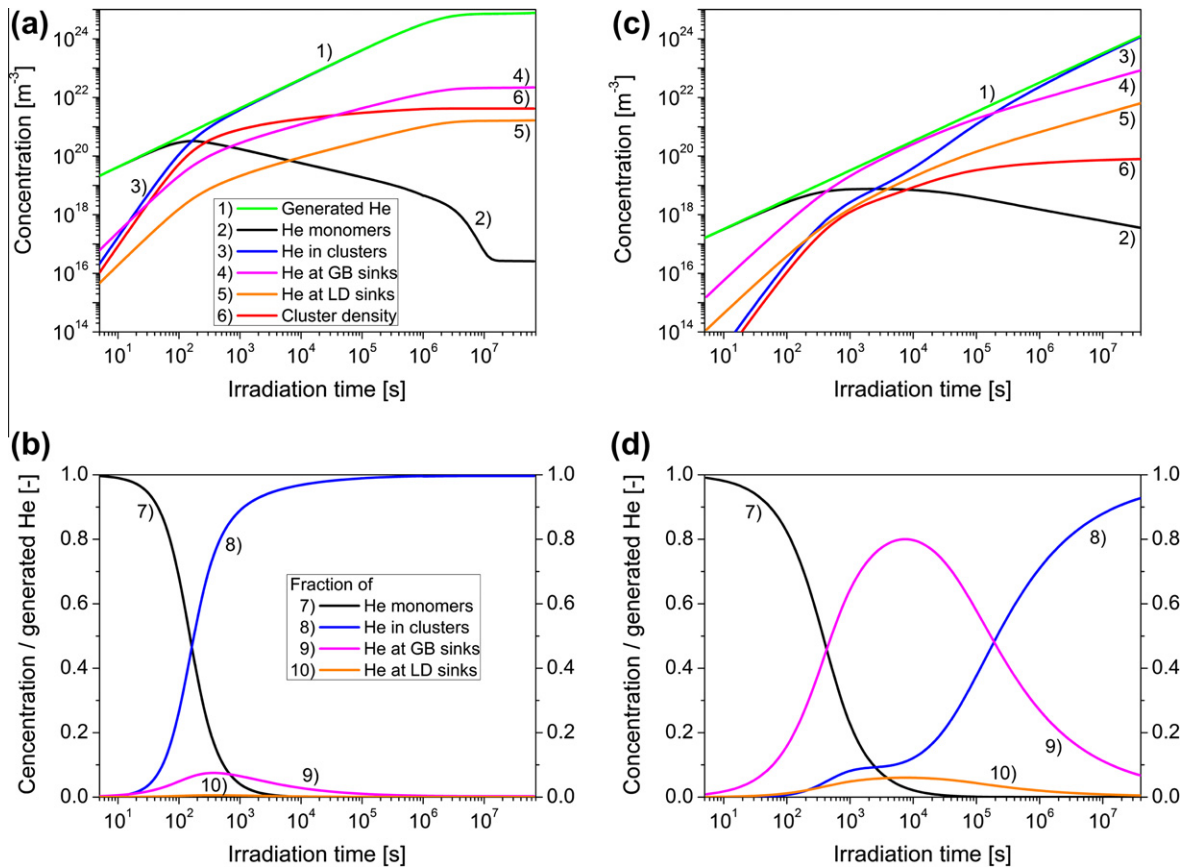


Fig. 7. Comparison of concentration evolution for ADS2 in SPICE (a and b) and ARBOR1 (c and d) for $x_{\text{He}} = 1$, taking into account grain boundaries (GB) and line dislocations (LD) as helium sinks. Top diagrams present concentration evolutions with absolute values, while the lower diagrams show concentrations normalized to the helium concentration generated so far.

3.7. Influence of helium density inside bubbles

The effect on bubble evolution of varying helium densities, i.e. helium-to-vacancy ratios x_{He} , inside the bubbles is examined. Since overpressurized bubbles are less likely, bubble size distributions calculated for ADS2 and ADS3 under ARBOR1 conditions are compared for helium-to-vacancy ratios of 1 and 0.5 in Fig. 8. Simulation results show that final peak bubble diameters are smaller for $x_{\text{He}} = 0.5$. The peak shift compared to $x_{\text{He}} = 1$ is larger for ADS2 than for ADS3, in the latter case diameters almost coincide at

~7.8 nm. In both cases cluster densities for small bubble sizes are much higher for $x_{\text{He}} = 0.5$.

The time evolution of the size distribution shows a different behavior for different helium-to-vacancy ratios: at the start of the irradiation nucleating bubbles for $x_{\text{He}} = 0.5$ are larger due to their lower packing fraction. At 10^6 s, the peak diameters are still larger, whereas after 3.98×10^7 s they are slightly smaller than for $x_{\text{He}} = 1$ due to a higher growth rate in the latter case.

4. Helium induced hardening

Obstacles impede dislocation glide and therefore lead to hardening and thus an increase in yield strength. Hardening due

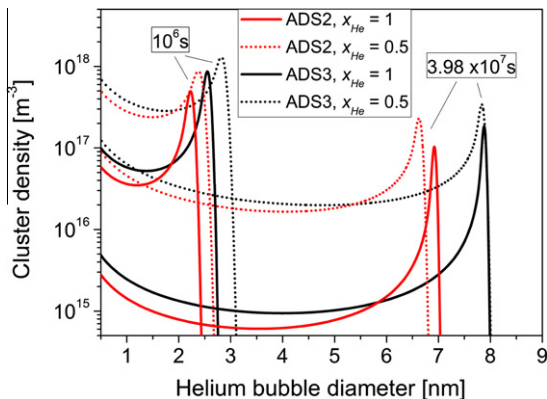


Fig. 8. Helium bubble size distributions, calculated for ADS2 and ADS3 in ARBOR1 irradiation experiment. Simulations are performed with varying helium-to-vacancy ratio x_{He} , and results are shown for two different irradiation times.

Table 6

Helium induced hardening $\Delta\sigma_{\text{He}}$ using simulated size distributions from SPICE and ARBOR1 irradiation ($x_{\text{He}} = 1$, if not mentioned otherwise). Differences in hardening when taking into account sinks and varying the helium-to-vacancy ratio are shown. The range of the hardening values stems from varying the barrier strength α from 0.2 to 0.4.

	$\Delta\sigma_{\text{He}}$ (MPa)	
	ADS2	ADS3
<i>SPICE</i>		
sim.	44–89	79–159
sim. ($x_{\text{He}} = 0.5$)	49–97	86–173
<i>ARBOR1</i>		
sim.	9–18	14–28
sim. (+ sinks)	8–16	14–27
sim. ($x_{\text{He}} = 0.5$)	14–28	21–43

to helium bubbles can be described by the Dispersed Barrier Hardening (DBH) model [54–56], where obstacles are considered homogeneously distributed in the matrix. Helium bubbles are treated as short range obstacles, which directly influence dislocation movement only on the dislocation glide planes, with no long range induced stresses on elastic lattice properties. Taking into account bubble sizes ($2R_i$) and densities (C_i) the increase in yield strength is described by the equation

$$\Delta\sigma_{\text{He}} = M_T \alpha \mu b_{\text{dist}} \sqrt{\sum_{i=1}^{i_{\text{max}}} 2R_i C_i}. \quad (28)$$

In this equation, M_T is the Taylor factor, giving the relation of shear stress on a glide plane in a single crystal to tensile stress necessary to activate slip in a polycrystal, α is the barrier strength of helium bubbles, μ is the shear modulus of the steel, and b_{dist} is the Burgers vector of the primary glide dislocations.

The DBH model is applied to the simulated helium bubble size distributions shown in Fig. 6. Parameters are taken from [51,53], while the barrier strength α for helium bubbles is taken as a fit parameter in the range between 0.2 and 0.4, which classifies helium bubbles as weak/intermediate obstacles to dislocation glide. Table 6 shows results of simulated hardening due to helium bubbles for both boron doped steels. For ARBOR1, hardening was additionally calculated taking into account effects of sinks.

Hardening calculated with helium bubble size distributions for the ARBOR1 experiment yielded 9–18 and 14–28 MPa for ADS2 and ADS3, respectively. Hardening results slightly decrease when GB and LD sinks are taken into account due to the change in cluster size distributions (Fig. 6). For a helium-to-vacancy ratio of 0.5, simulations for ARBOR1 show an increased expected hardening between 14–28 MPa for ADS2 and 21–43 MPa for ADS3. In SPICE, a relatively small change of hardening for $x_{\text{He}} = 0.5$ is observed.

5. Discussion

As shown in Section 3, the developed model is suitable to calculate helium cluster size distributions for different helium production rates and for timescales relevant to high dose irradiation experiments. The basic model is adapted to the irradiation experiments SPICE and ARBOR1. Temperature dependent parameters are described and validated by literature studies. Although quantitative measurements of helium bubble densities and sizes are not yet completed, the peaks of calculated cluster size distributions are in close agreement with data from SPICE experiment [13].

Limitations of the model are given by some of the assumptions done. The calculations are performed for fixed helium-to-vacancy ratios in the bubbles being of the order of unity. Though this assumption is generally not valid, it is still a good approximation for the description of bubble growth at the stage preceding bubble-to-void transformation. Furthermore, only helium monomers are considered to be mobile in the matrix. Therefore helium bubble coalescence is not taken into account and possible coarsening mechanisms are reduced. Coarsening would be relevant to describe especially at later stages of irradiation experiments when helium generation by boron transmutation ceases. Only little change in cluster size distributions can be observed between 10^7 s and the end of SPICE irradiation program at 6.67×10^7 s, because the contribution of the helium generation by steel matrix atoms is small, yielding only 7 appm helium for this long irradiation period. By contrast, transmutation of helium matrix elements gains importance the lower the boron transmutation rates and associated total helium amounts are, as in the case of ADS2 under ARBOR1 irradiation.

Emission rates of helium atoms from existing clusters depend on helium solubility in the matrix. Due to the low temperature irradiation conditions with helium trapped as a substitutional atom, substitutional helium solubility is used to calculate emission rates. Although substitutional solubility is much higher than the interstitial one, resulting equilibrium concentrations are very low. The reason why emission rates nevertheless play an important role in the presented model (as it was shown in Fig. 5) is due to the surface energy, whose exponential dependency on the emission rate is responsible for the change in bubble size distributions. Since temperature dependent helium solubility is calculated by using ideal gas approximation, possible uncertainties are parametrically studied in a first attempt by increasing and decreasing solubility by one order of magnitude, achieving peak bubble diameters for ADS3 in ARBOR1 of 10.1 and 6.6 nm, respectively, while standard values yield 7.9 nm.

An interesting point is given by the description of the helium losses to sinks. While the helium monomer concentration in the matrix is lowered by the fraction of helium atoms diffusing to sinks, the helium is not lost, but stored at the different sink sites. Therefore, depending on the sink strengths, the sinks themselves may act as nucleation sites for further helium clustering. While the creation of helium bubbles described by the model is based on homogeneous nucleation in the matrix, clustering at sinks must be attributed to a heterogeneous type. Recalling the TEM micrographs cited in Section 1, heterogeneous distribution of helium bubbles concentrated at sinks, e.g. line dislocations or grain boundaries, might be explained as follows: If the sink strength is strong enough, the main fraction of helium atoms will diffuse to the sinks and the remaining helium concentration in the matrix will be small, leading to a primary bubble nucleation at sink sites. Temperature plays a dominant role in this process, because of the strong temperature dependence of the helium diffusivity. That is why at higher temperatures a greater influence of heterogeneous nucleation is expected [27]. In the next step the simulation model will be extended to the description of helium bubble nucleation and growth at sinks.

The helium density inside a bubble, i.e. helium-to-vacancy ratio x_{He} , has an important influence on the calculated bubble size distributions. Values of x_{He} were defined as 0.5 and 1, demonstrating the influence of x_{He} within realistic ranges expected from results of TEM measurements. Since a size independent x_{He} is only an assumption, further simulation attempts will use equation of states for helium bubbles, e.g. as it was recently proposed in [57]. Interestingly, simulation results obtained for ADS2 and ADS3 under ARBOR1 irradiation conditions showed peak bubble diameters which do not differ much between $x_{\text{He}} = 0.5$ and 1. Due to the evolution of the bubble size distributions from 10^6 to 3.98×10^7 s, further irradiation would advance the evolution for $x_{\text{He}} = 1$ much faster, increasing the peak shift between the different helium-to-vacancy ratios. A lower x_{He} leads to a high concentration of medium sized clusters, whose density is less by only one order of magnitude from the peak density, while for $x_{\text{He}} = 1$ the difference is more than two orders of magnitude at the end of irradiation.

Assessment of helium induced hardening was performed for simulated bubble size distributions using the DBH model. As mentioned in Section 1, hardening due to helium only shows a minor contribution to the overall hardening. While simulated helium bubble size distributions alone would cause the hardening calculated in Table 6, superposition effects with other obstacles types have to be considered. The calculated hardening is in good agreement with an experimentally observed extra hardening in ADS2 (SPICE, 40 MPa) and in ADS3 (SPICE, 92 MPa). The direct comparison of helium hardening will however imply a linear superposition law of hardening contributions between helium bubbles and other

obstacle types. In the case of application of a square root superposition law [58] the calculated helium hardening will strongly underestimate the experimentally observed extra hardening by taking into account irradiation induced (non-helium) hardening of base EUROFER97 steel (405 MPa).

Below, the irradiation programs SPICE and ARBOR1 are analyzed with respect to expected fusion conditions. To gain high energy efficiency, the temperature in the First Wall of the reactor has to be as high as possible to offer a large temperature range for the cooling medium, but it is limited by the maximum operation temperature of the steel. For EUROFER97, the upper application limit is given by the creep strength, which is acceptable up to 550 °C [59]. Minimum temperatures should not fall below 350 °C, because otherwise a large embrittlement is expected. In fusion power plants, dose rates between 20 and 30 dpa/year with helium generation rates from 10 to 15 appm/dpa are expected in the First Wall. Transmutation rates are assumed to remain unchanged with time due to a high fraction of helium producing isotopes, e.g. the stable isotope ^{54}Fe is enclosed at a percentage of 5.8% within iron and producing helium by an (n,α)-reaction. These conditions will result in helium concentrations of 200–450 appm/year. While in ARBOR1 a constant helium generation rate was achieved, the produced helium amount per year (~ 40 appm for ADS3) is too low when compared to fusion conditions. The helium concentration after the first year of irradiation in SPICE (~ 435 appm for ADS3) fits within the range of the expected helium amount under fusion neutrons, but the transmutation rate is not constant. While temperatures in ARBOR1 cover the lower regime of expected First Wall temperatures, the SPICE experiment took place within a temperature range of 250 and 450 °C. In comparison to ARBOR1 the diffusivity of helium is estimated to be two orders of magnitude higher at 550 °C. Although both irradiation experiments cannot accurately describe the conditions expected in the First Wall of future fusion reactors, they present a wide range of irradiation conditions which allow to adapt and validate the developed model. After validation and refinement the behavior of RAFM steels under expected fusion conditions will be simulated.

6. Summary

In this work the following achievements are presented:

- A phenomenological model was developed based on kinetic rate equations to describe helium bubble formation and growth in RAFM steels under neutron irradiation. The model was adapted to different ^{10}B doped specimens irradiated in SPICE and ARBOR1 experiments.
- A Fortran code was built up to numerically solve the kinetic rate equations. Modifications were implemented to assure stable and sufficiently fast calculations.
- The concentration evolution at small irradiation times showed that the modeled nucleation mechanism satisfies the conditions for di-atomic nucleation.
- The influence of the surface energy on the emission rate constant and hence the final cluster size distribution was determined. Using literature values for the iron surface energy yielded a size-dependent cluster resolution with a shift of the cluster size distribution towards larger sizes.
- The influences of grain boundaries and line dislocations acting as sinks for helium were investigated. Higher irradiation temperatures and lower helium generation rates promote helium capturing by sinks. Due to the sinks' influence on nucleation, final cluster size distributions are broadened and the peak bubble diameter is shifted towards larger sizes. The largest effect was shown for the low ^{10}B doped steel ADS2, where 7.2% of

the totally generated helium is expected to be situated at sinks at the end of the ARBOR1 experiment.

- Simulations reveal final peak bubble diameters of 3.7 and 4.6 nm for ADS2 and ADS3 in SPICE, and 6.9 and 7.9 nm in ARBOR1 (7.3 and 8.1 nm when taking into account sinks). These results agree qualitatively well with TEM investigations on SPICE specimens in the literature.
- Variation of helium-to-vacancy ratio showed minor effect on peak bubble diameters at the end of ARBOR1 experiment, but enormously increased concentrations of smaller sized bubbles using a lower x_{He} of 0.5.
- Helium induced hardening was determined by applying the Dispersed Barrier Hardening model to the calculated cluster size distributions. For a size-invariant barrier strength simulated hardening was compared to experimental results. Good agreement was achieved by assuming a linear superposition of helium induced hardening with hardening from other obstacle types.

Quantitative TEM investigations are scheduled and will be performed to validate the simulation results. Future work will consider helium clustering at sinks. Finally, simulations will predict conditions as they are expected in the First Wall of future fusion reactors.

Acknowledgments

This work has been supported by Helmholtz Association and Russian Foundation for Basic Research in the framework of the joint research group HRJRG-013.

This work, supported by the European Communities under the contract of Association between EURATOM and Karlsruhe Institute of Technology, was carried out within the framework of the European Fusion Development Agreement. The views and opinions expressed herein do not necessarily reflect those of the European Commission.

References

- [1] K. Mergia, N.M. Boukos, *Journal of Nuclear Materials* 373 (2008) 1–8.
- [2] P. Graf, H. Zimmermann, E. Nold, E. Materna-Morris, A. Möslang, *Sonderbände der Praktischen Metallographie* 35 (2004) 71–76.
- [3] Y. Dai, W. Wagner, *Journal of Nuclear Materials* 389 (2009) 288–296.
- [4] R.L. Klueh, N. Hashimoto, M.A. Sokolov, P.J. Maziasz, K. Shiba, S. Jitsukawa, *Journal of Nuclear Materials* 357 (2006) 169–182.
- [5] E. Wakai, S. Jitsukawa, H. Tomita, K. Furuya, M. Sato, K. Oka, T. Tanaka, F. Takada, T. Yamamoto, Y. Kato, Y. Tayama, K. Shiba, S. Ohnuki, *Journal of Nuclear Materials* 343 (2005) 285–296.
- [6] A. Möslang, *Comptes Rendus Physique* 9 (2008) 457–468.
- [7] J. Ahlf, R. Conrad, G.P. Tartaglia, G. Tsotridis, *Journal of Nuclear Materials* 212–215 (1994) 1635–1639.
- [8] E. Gaganidze, H.-C. Schneider, B. Dafferner, J. Aktaa, *Journal of Nuclear Materials* 367–370 (2007) 81–85.
- [9] C. Petersen, V. Shamardin, A. Fedoseev, G. Shimansky, V. Efimov, J.W. Rensman, *Journal of Nuclear Materials* 307–311 (2002) 1655–1659.
- [10] E. Gaganidze, J. Aktaa, *Fusion Engineering and Design* 83 (2008) 1498–1502.
- [11] O.J. Weiß, Private Communication, 2009–2011. Karlsruhe Institute of Technology, Institute for Applied Materials, Karlsruhe, Germany, 2011.
- [12] E. Materna-Morris, A. Möslang, H.-C. Schneider, R. Rolli, in: *Proceedings of 22nd IAEA Fusion Energy Conference FT/P2-2*, 2008, pp. 1–5.
- [13] E. Materna-Morris, J. Aktaa, B. Dafferner, J. Ehrmann, E. Gaganidze, M. Holzer, S. Lautensack, A. Möslang, H. Ries, R. Rolli, H.-C. Schneider, *Forschungszentrum Karlsruhe FZKA 7383* (2008) 129–133.
- [14] E. Gaganidze, C. Dethloff, O.J. Weiß, V. Svetukhin, M. Tikhonchev, J. Aktaa, in: *25th ASTM Symposium on Effects of Radiation on Nuclear Materials*, June 15th–17th, 2011, Anaheim, USA.
- [15] E. Gaganidze, C. Petersen, E. Materna-Morris, C. Dethloff, O. Weiß, J. Aktaa, A. Povstnyanko, A. Fedoseev, O. Makarov, V. Prokhorov, *Journal of Nuclear Materials* 417 (2011) 93–98.
- [16] R. Kurtz, A. Alamo, E. Lucon, Q. Huang, S. Jitsukawa, A. Kimura, R. Klueh, G. Odette, C. Petersen, M. Sokolov, P. SpStig, J.-W. Rensman, *Journal of Nuclear Materials* 386–388 (2009) 411–417.
- [17] S.L. Dudarev, J.-L. Boutard, R. Lässer, M.J. Caturia, P.M. Derlet, M. Fivel, C.-C. Fu, M.Y. Lavrentiev, L. Malerba, M. Mrovec, D. Nguyen-Manh, K. Nordlund, M.

- Perlado, R. Schäublin, H. Van Swygenhoven, D. Terentyev, J. Wallenius, D. Weygand, F. Willaime, *Journal of Nuclear Materials* 386–388 (2009) 1–7.
- [18] C.-C. Fu, F. Willaime, *Physical Review B* 72 (2005) 064117–6.
- [19] V.A. Borodin, P.V. Vladimirov, *Journal of Nuclear Materials* 386–388 (2009) 106–108.
- [20] R.J. Kurtz, H.L. Heinisch, F. Gao, *Journal of Nuclear Materials* 382 (2008) 134–142.
- [21] B.D. Wirth, G.R. Odette, J. Marian, L. Ventelon, J.A. Young-Vandersall, L.A. Zepeda-Ruiz, *Journal of Nuclear Materials* 329–333 (2004) 103–111.
- [22] N.M. Ghoniem, M.L. Takata, *Journal of Nuclear Materials* 105 (1982) 276–292.
- [23] L.K. Mansur, W.A. Coghlan, *Journal of Nuclear Materials* 119 (1983) 1–25.
- [24] N.M. Ghoniem, S. Sharafat, J.M. Williams, L.K. Mansur, *Journal of Nuclear Materials* 117 (1983) 96–105.
- [25] F.F. Abraham, *Homogeneous Nucleation Theory – The Pretransition Theory of Vapor Condensation*, Academic Press Inc., 1974.
- [26] S. Fréhard, M. Walls, M. Kociak, J.P. Chevalier, J. Henry, D. Gorse, *Journal of Nuclear Materials* 393 (2009) 102–107.
- [27] H. Trinkaus, B.N. Singh, *Journal of Nuclear Materials* 323 (2003) 229–242.
- [28] K. Morishita, *Philosophical Magazine* 87 (2007) 1139–1158.
- [29] D. Terentyev, N. Juslin, K. Nordlund, N. Sandberg, *Journal of Applied Physics* 105 (2009) 103509–103512.
- [30] C.J. Ortiz, M.J. Caturla, C.C. Fu, F. Willaime, *Physical Review B* 75 (2007) 100102–100104.
- [31] S.V. Bulyarskii, V.V. Svetukhin, O.V. Prikhod'ko, *Semiconductors* 33 (1999) 1157–1162.
- [32] P. Pichler, *Intrinsic Point Defects, Impurities, and Their Diffusion in Silicon*, Computational Microelectronics, Springer-Verlag, Wien, 2004.
- [33] C.J. Ortiz, P. Pichler, T. Fuhner, F. Cristiano, B. Colombeau, N.E.B. Cowern, A. Claverie, *Journal of Applied Physics* 96 (2004) 4866–4877.
- [34] G.S. Was, *Fundamentals of Radiation Materials Science*, Springer-Verlag, 2007.
- [35] R.T. DeHoff, *Thermodynamics in Materials Science*, second ed., CRC Press, 2006.
- [36] A. Gokhman, F. Bergner, A. Ulbricht, U. Birkenheuer, *Defect and Diffusion Forum* 277 (2008) 75–80.
- [37] A. Gokhman, F. Bergner, A. Ulbricht, *FZ-Dresden 04-R13* (2009) 76–81.
- [38] W.R. Tyson, W.A. Miller, *Surface Science* 62 (1977) 267–276.
- [39] V.V. Slezov, J.W.P. Schmelzer, A.S. Abyzov, *Nucleation Theory and Applications*, Wiley-VCH, 2005.
- [40] R. Kemp, G. Cottrell, K.D.H. Bhadeshia, *Energy Materials: Materials Science and Engineering for Energy Systems* 1 (2006) 103–105.
- [41] H. Ullmaier, *The Landolt-Börnstein Database 25: Atomic Defects in Metals* (2010) 380–437.
- [42] L. Yang, X.T. Zu, H.Y. Xiao, F. Gao, H.L. Heinisch, R.J. Kurtz, *Physica B: Condensed Matter* 391 (2007) 179–185.
- [43] P.G. Klemens, B. Cort, *Journal of Alloys and Compounds* 252 (1997) 157–161.
- [44] G.R. Odette, M.J. Alinger, B.D. Wirth, *Annual Review of Materials Research* 38 (2008) 471–503.
- [45] L.K. Mansur, *Kinetics of Nonhomogeneous Processes – 8, Mechanisms and Kinetics of Radiation Effects in Metals and Alloys*, Wiley Interscience Publication, 1987.
- [46] F.A. Nichols, *Journal of Nuclear Materials* 75 (1978) 32–41.
- [47] A.D. Brailsford, R. Bullough, *Mathematical and Physical Sciences* (1934–1990) 302 (1981) 87–137.
- [48] M. Rieth, B. Dafferner, H.D. Röhrig, *Journal of Nuclear Materials* 258–263 (1998) 1147–1152.
- [49] L.R. Greenwood, B.M. Oliver, S. Ohnuki, K. Shiba, Y. Kohno, A. Kohyama, J.P. Robertson, J.W. Meadows, D.S. Gelles, *Journal of Nuclear Materials* 283–287 (2000) 1438–1442.
- [50] G. Shimansky, Private Communication, 2007. SSC RIAR, Dimitrovgrad, Russia.
- [51] G. Speich, A. Schwoeble, W. Leslie, *Metallurgical and Materials Transactions B* 3 (1972) 2031–2037.
- [52] M. Rieth, M. Schirra, A. Falkenstein, P. Graf, S. Heger, H. Kemp, R. Lindau, H. Zimmermann, *Wissenschaftliche Berichte FZKA* 6911 (2003) 1–83.
- [53] N. Hashimoto, T.S. Byun, K. Farrell, S.J. Zinkle, *Journal of Nuclear Materials* 336 (2005) 225–232.
- [54] G.E. Lucas, *Journal of Nuclear Materials* 206 (1993) 287–305.
- [55] F.A. Garner, M.L. Hamilton, N.F. Panayotou, G.D. Johnson, *Journal of Nuclear Materials* 104 (1981) 803–807.
- [56] J. Gan, G.S. Was, *Journal of Nuclear Materials* 297 (2001) 161–175.
- [57] A. Caro, J. Hetherly, A. Stukowski, M. Caro, E. Martinez, S. Srivilliputhur, L. Zepeda-Ruiz, M. Nastasi, *Journal of Nuclear Materials* 418 (2011) 261–268.
- [58] M. Lambrecht, E. Meslin, L. Malerba, M. Hernández-Mayoral, F. Bergner, P. Pareige, B. Radigue, A. Almazouzi, *Journal of Nuclear Materials* 406 (2010) 84–89.
- [59] N. Baluc, *Plasma Physics and Controlled Fusion* 48 (2006) B165–B177.